Accurate Shot-Noise-Limited Calibration of a Time-Domain Balanced Homodyne Detector for Continuous-Variable Quantum Key Distribution

Xu-Yang Wang, Xu-Bo Guo, Yan-Xiang Jia, Yu Zhang, Zhen-Guo Lu, Jian-Qiang Liu, and Yong-Min Li

***Abstract*—The time-domain balanced homodyne detector (TBHD) is critical component in continuous-variable quantum key distribution (CVQKD). The shot-noise-limited attribute of a TBHD depends on the whole frequency spectrum of the detector, in contrast to a frequency-domain balanced homodyne detector that focuses only on part of the frequency spectrum. We propose a method for accurate calibration of the shot-noise-limited attribute of the TBHD by overlapping the gain lines of the TBHD and an integral photodetector which is realized by blocking one photodiode of the TBHD. The overlapping of two lines indicates that the detector is indeed shot noise limited, which is crucial to the security of CVQKD. Experimentally, we use this method to obtain a calibration error of ±1‰. Theoretical analysis showed that the CVQKD security is very sensitive to calibration errors of shot noise, and proper countermeasure was proposed to eliminate this issue. The presented methods are expected to contribute to CVQKD security and TBHD standardization.**

***Index Terms*—Continuous-variable quantum key distribution, Time-domain balanced homodyne detector, Shot-noise-limited calibration.**

I. Introduction

THE balanced homodyne detector (BHD) plays an important role in quantum information field [1], [2]. Its applications include measurement of squeezed and entanglement states [3], [4], [5], [6], [7], [8], [9], continuous-variable quantum teleportation and steering [10], [11], [12], [13], [14], [15], quantum random number generation [16], [17], [18], [19], [20], quantum tomography, and continuous-variable quantum key distribution (CVQKD) using a continuous beam [21], [22], [23], [24], [25]. The above experiments usually used a frequency-domain BHD (FBHD), which measures a continuous beam and focuses on only part of the frequency spectrum of the detector output. In 1993, Raymer et al. designed a time-domain BHD (TBHD), which is important for quantum tomography and CVQKD using a pulsed beam [26], [27], [28], [29], [30], [31], [32], [33], [34], [35], [36], [37], [38]. A TBHD can integrate each laser pulse and output a field quadrature signal, which covers the whole spectrum range of detector. What's more important is that the TBHD is compatible with photon counting technology, or it can be used to detect signal beam with intensity on the order of single-photon level. Along with it is that there will be critical technical challenges, such as high common mode rejection ratio (CMRR) requirement, calibration of the shot-noise-limited attribute [39].

Quantum key distribution is a key technology in quantum communication owing to its unconditional security in information theory [40], [41], [42], [43], [44], [45]. Depending on the measurement method, it can be divided into discrete- and continuous-variable domains. In 1984, the BB84 protocol, which uses a single-photon detector, was proposed for the discrete-variable domain [46]. Up to now, a maximum transmission distance of 830 km in fiber has been achieved [47], and a satellite-ground platform has been demonstrated in this domain [48]. In 2002, the GG02 protocol using a TBHD was proposed for the continuous-variable domain [29], and demonstration experiment was performed in 2003 [31]. The GG02 protocol utilizes only the coherent state and does not require the squeezed or entangled states, so it has good compatibility with classical coherent communication technology. It has achieved a maximum transmission distance of 200 km [37], and is expected to be employed for quantum private networks in metropolitan areas.

In CVQKD, the quadratures of the signal field measured by the receiver are normalized to the shot noise, which can be determined by the power of the local oscillator (LO). To this end, a linear relationship between the shot noise variance and LO's power is calibrated before operation of a CVQKD system. Inaccurate calibration of the slope of the line will lead to security

Manuscript received 31 July 2022; revised 27 February 2023 and 22 March 2023; accepted 28 March 2023. Date of publication 3 April 2023; date of current version 4 September 2023. This work was supported in part by the Key Research and Development Program of Guangdong Province under Grant 2020B0303040002, in part by the Research Project Supported by Shanxi Scholarship Council of China under Grant 2022-016, in part by the Aeronautical Science Foundation of China under Grant 20200020115001, in part by the National Natural Science Foundation of China under Grant 62175138, in part by the Shanxi 1331KSC, in part by the Provincial Natural Science Foundation of Shanxi, China under Grant 202103021224010, and in part by the Innovation Program for Quantum Science and Technology under Grant 2021ZD0300703. *(Corresponding authors: Xu-Yang Wang; Yong-Min Li.)*

Xu-Yang Wang and Yong-Min Li are with the State Key Laboratory of Quantum Optics and Quantum Optics Devices, Institute of Opto-Electronics, Shanxi University, Taiyuan 030006, China, also with the Collaborative Innovation Center of Extreme Optics, Shanxi University, Taiyuan 030006, China, and also with the Hefei National Laboratory, Hefei 230088, China (e-mail: wangxuyang@sxu.edu.cn; yongmin@sxu.edu.cn).

Xu-Bo Guo, Yan-Xiang Jia, Yu Zhang, Zhen-Guo Lu, and Jian-Qiang Liu are with the State Key Laboratory of Quantum Optics and Quantum Optics Devices, Institute of Opto-Electronics, Shanxi University, Taiyuan 030006, China (e-mail: 775771537@qq.com; jiayanxiang5806@163.com; zhangyu_04@163.com; zglu@sxu.edu.cn; jq-liu@foxmail.com).

Color versions of one or more figures in this article are available at https://doi.org/10.1109/JLT.2023.3264234.

Digital Object Identifier 10.1109/JLT.2023.3264234

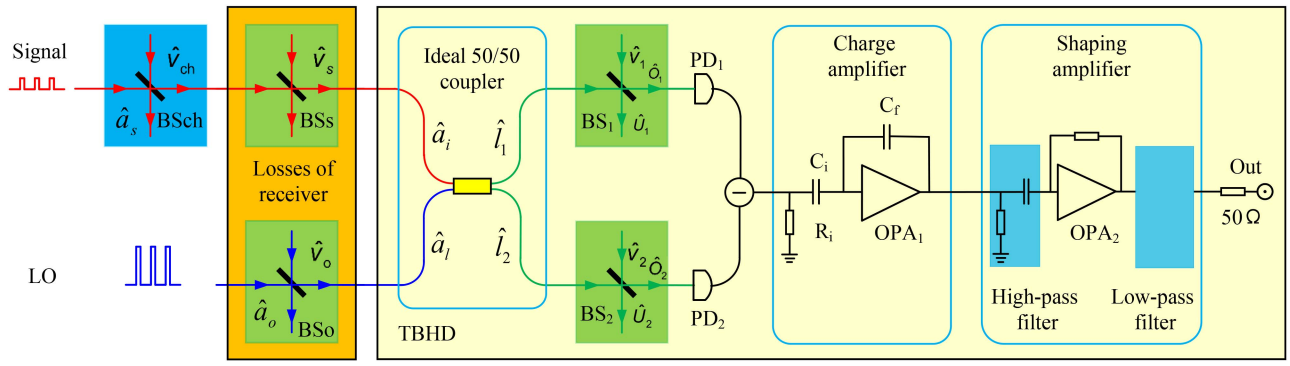

Fig. 1. Accurate model of the TBHD and relevant losses in CVQKD systems.

loopholes. Calibration of the shot noise is the main difference between CVQKD and a coherent optical communication system, which utilizes an FBHD to measure the quadrature of electromagnetic modes to transmit information [49]. An FBHD only considers part of the frequency spectrum, and the shot-noise-limited attribute can be verified by using a standard radio frequency (RF) spectrometer [50]. This method is not suitable for TBHD which is used to detect pulsed beam. For a TBHD, the entire spectral range should be verified to be shot-noise-limited, especially at low frequencies. Due to limited CMRR, the low frequency intensity noise of LO pulse is difficult to be eliminated totally. The intensity noises of the LO pulse mainly come from the laser intensity noise and modulation process.

To achieve a high CMRR and minimize the low-frequency remaining intensity noise for a TBHD, several techniques are utilized. For example, two matched photodiodes with adjustable bias voltages are employed and the output optical paths of the 50/50 coupler are set to be identical [39], [51], [52], [53]. Low noise pulsed modulation technology is also needed to calibrate a TBHD [54]. However, the variance of the output quadrature may still be mixed with the remaining intensity noise because of the limited CMRR. Thus, a linear relationship between the quadrature variance and LO power is not enough to make sure the TBHD is shot-noise-limited.

In this study, an accurate model for a TBHD was established, and the shot noise calibration process was analyzed in detail. A method is proposed for verifying the shot-noise-limited attribute by overlapping the fitting gain lines of the TBHD and the integral photodetector which is realized by blocking one photodiode of the TBHD. When the two gain lines overlap, the remaining intensity noise of output quadrature variance has been eliminated and the TBHD can be considered to be shot-noise-limited. Experiments were performed to validate the model and calibration performance, and a theoretical analysis is presented on the effects of inaccurate calibration on a CVQKD system. Finally, the countermeasures of decreasing the safe line of the TBHD is recommended to avoid security loophole due to inevitable calibration errors.

II. Model of the TBHD

An accurate model of the TBHD was established to clarify the calibration process as shown in Fig. 1. The signal pulse $\hat{a}_i$ and LO pulse $\hat{a}_l$ interfere at an ideal 50/50 coupler, and the output beams $\hat{l}_1$ and $\hat{l}_2$ are guided into two ideal photodiodes PD_1 and PD_2, both have quantum efficiencies of 100%. The paths from the coupler to PD_1 and PD_2 are denoted as paths 1 and 2, respectively. Beam splitters (BS) are used to model the losses of realistic couplers. PD_1 and PD_2 convert the input photons into photoelectrons, which are subtracted from each other. The subtracted photoelectrons are amplified by the charge amplifier and shaping amplifier, which consist of a high-pass filter, low noise-operation amplifier (OPA), and low-pass filter. R_i is the input resistor, C_i is the input capacitor, and C_f is the feedback capacitor. The output impedance of the TBHD is 50Ω. This interference of the signal beam $\hat{a}_i$ and LO beam $\hat{a}_l$ can be described as follows

$$\begin{bmatrix} \hat{l}_1 \\ \hat{l}_2 \end{bmatrix} = \begin{bmatrix} 1/\sqrt{2} & 1/\sqrt{2} \\ 1/\sqrt{2} & -1/\sqrt{2} \end{bmatrix} \cdot \begin{bmatrix} \hat{a}_i \\ \hat{a}_l \end{bmatrix}, \tag{1}$$

where the beams $\hat{l}_1$ and $\hat{l}_2$ have photon numbers $\hat{n}_1 = \hat{l}_1^\dagger \hat{l}_1$ and $\hat{n}_2 = \hat{l}_2^\dagger \hat{l}_2$, respectively. In the idea case, the ideal photodiodes transform $\hat{n}_1$ and $\hat{n}_2$ photons into $\hat{n}_{e1}$ and $\hat{n}_{e2}$ photoelectrons, respectively, with perfect 100% efficiency. The subtracted photoelectrons $\hat{N}_r$ are given by

$$\begin{aligned} \hat{N}_r &= \hat{n}_{e1} - \hat{n}_{e2} = \hat{n}_1 - \hat{n}_2 \\ &= \hat{a}_i^\dagger \hat{a}_l + \hat{a}_i \hat{a}_l^\dagger = |\beta| \cdot \left(\hat{a}_i^\dagger \cdot e^{i\theta_i} + \hat{a}_i \cdot e^{-i\theta_i} \right) \\ &= |\beta| \cdot \hat{X}_{\theta_i}. \end{aligned} \tag{2}$$

Here we have treated the strong LO beam as classical field $\beta = |\beta| \cdot e^{i\theta_i}$, where $|\beta|$ represents the amplitude of the LO beam and θ_i is the phase of the LO beam, $\hat{X}_{\theta_i}$ is the quadrature. Then, the subtracted photoelectrons $\hat{N}_r$ are amplified by the following amplifiers with gain G. The peak value of the output voltage is given by

$$\hat{U}_{peak} = G \cdot |\beta| \cdot \hat{X}_{\theta_i}. \tag{3}$$

When the signal beam is in vacuum, the variance of the output peak value is

$$V_{peak} = G^2 \cdot |\beta|^2 \cdot \left\langle \Delta^2 \hat{X}_{\theta_i} \right\rangle = G^2 \cdot |\beta|^2. \tag{4}$$

Here, the variance $\left\langle \Delta^2 \hat{X}_{\theta_i} \right\rangle$ of the vacuum field is set to 1. The variance V_{peak} has linearity dependence with the photon number

per LO pulse $|\beta|^2$, and the slope is G^2. In the above derivation, $\hat{N}_r$ represents the total subtracted photoelectrons number per LO pulse. The instantaneous subtracted photoelectrons current is defined as $\hat{i}_r(t)$. The charge amplifiers integrate $\hat{i}_r(t)$ over the duration time T of the pulsed photoelectrons current, which can be expressed by

$$\hat{U}_{peak} = G \cdot \hat{N}_r = G \cdot \int_0^T \hat{i}_r(t)dt = G \cdot \int_0^T \left(\hat{i}_{e1}(t) - \hat{i}_{e2}(t)\right)dt. \quad (5)$$

The duration time T should be much shorter than the time constant of the charge amplifier. (5) can be rewritten as

$$\hat{U}_{peak} = G \cdot \hat{N}_r = G \cdot (\hat{n}_{e1} - \hat{n}_{e2}). \quad (6)$$

When one photodiode of the TBHD is blocked, it is can be considered to be an integral photodetector. All of the photoelectrons $\hat{N}_i$ of one photodiode are integrated and the output peak voltage is

$$\hat{U}_p = G \cdot \hat{N}_i = (-1)^{i+1} G \cdot \int_0^T \hat{i}_{ei}(t)dt, (i = 1, 2). \quad (7)$$

The gain G can also be measured by using the integral photodetector. Note that an FBHD can also be used to detect the pulsed light. However, there is no charge amplifier. Normally, a transimpedance amplifier with a feedback resistor R is used to amplify the subtracted current signal directly. When the duration time of the optical pulse is much greater than the response time of the FBHD, the output voltage is given by

$$\hat{U}_r(t) = \hat{i}_r(t) \cdot R = \left[\hat{i}_{e1}(t) - \hat{i}_{e2}(t)\right] \cdot R. \quad (8)$$

To obtain the total subtracted number of photoelectrons with the gain R, which is given by $\hat{N}_r \cdot R$. A number of points should be sampled in a single signal pulse and then numerical integration is required to calculate the pulse area.

The above analysis shows that both the TBHD and FBHD can be used to detect the quadrature of a pulsed signal. The TBHD only needs to acquire the peak point, but the FBHD needs to acquire many samples and then integrating them, which increases the amount of data processing complexity.

A realistic 50/50 coupler may have a small deviation from the ideal coupler ratio of 1/2, and there may be losses when the signal beam $\hat{a}_i$ and LO beam $\hat{a}_l$ transmit through the 50/50 coupler. The four losses from beams $\hat{a}_i$, $\hat{a}_l$ to beams $\hat{l}_1$, $\hat{l}_2$ have slight discrepancies. The quantum efficiencies η_{PD1}, η_{PD2} of the two photodiodes also differ in general. To analyze various losses, a model was constructed under realistic conditions (see Appendix A). We find that the measurement of the shot noise depends on the detected photoelectrons number. To simplify the calibration process, the model in Fig. 1 can be transformed to have two output paths with the transmission efficiencies η_1 and η_2. When the two output paths are tuned to a balance, the two models are equivalent for the calibration of the shot-noise-limited attribute.

As shown in Fig. 1, BS_1 and BS_2, which model the transmission efficiencies η_1 and η_2, are placed on output paths 1 and 2, respectively. For path 1, beam $\hat{l}_1$ interferes with the signal beam in vacuum field $\hat{v}_1$. The output beams are $\hat{o}_1$ and $\hat{u}_1$. The incident photon number in PD_1 is given by

$$\hat{n}_1 = \hat{o}_1^\dagger \hat{o}_1 = (1-\eta_1) \cdot \hat{v}_1^\dagger \hat{v}_1 + \eta_1 \cdot \frac{1}{2}\left(\hat{a}_i^\dagger \hat{a}_i + \hat{a}_i^\dagger \hat{a}_l + \hat{a}_l^\dagger \hat{a}_i + \hat{a}_l^\dagger \hat{a}_l\right) + \sqrt{(1-\eta_1)\cdot\eta_1/2}\left(\hat{v}_1^\dagger \hat{a}_i + \hat{v}_1^\dagger \hat{a}_l + \hat{a}_l^\dagger \hat{v}_1 + \hat{a}_i^\dagger \hat{v}_1\right). \quad (9)$$

For path 2, the photon number received by PD_2 is given by

$$\hat{n}_2 = \hat{o}_2^\dagger \hat{o}_2 = (1-\eta_2) \cdot \hat{v}_2^\dagger \hat{v}_2 + \eta_2 \cdot \frac{1}{2}\left(\hat{a}_i^\dagger \hat{a}_i - \hat{a}_i^\dagger \hat{a}_l - \hat{a}_l^\dagger \hat{a}_i + \hat{a}_l^\dagger \hat{a}_l\right) + \sqrt{(1-\eta_2)\cdot\eta_2/2}\left(\hat{v}_2^\dagger \hat{a}_i - \hat{v}_2^\dagger \hat{a}_l - \hat{a}_l^\dagger \hat{v}_2 + \hat{a}_i^\dagger \hat{v}_2\right). \quad (10)$$

In experiment, a variable optical attenuator (VOA) based on bending the fiber can be inserted into one path with a higher transmission efficiency to balance the two paths [53]. For convenience, the transmission efficiencies of the two paths are assumed to be identical, or $\eta_1 = \eta_2 = \eta$. Then, the subtracted photoelectrons $\hat{N}_r$ are given by

$$\begin{aligned}\hat{N}_r &= \hat{n}_{e1} - \hat{n}_{e2} = \hat{n}_1 - \hat{n}_2 \\ &= (1-\eta) \cdot \left(\hat{v}_1^\dagger \hat{v}_1 - \hat{v}_2^\dagger \hat{v}_2\right) \\ &\quad + \sqrt{(1-\eta)\cdot\eta/2} \cdot \left(\hat{a}_i^\dagger \hat{v}_1 + \hat{v}_1^\dagger \hat{a}_i - \hat{a}_i^\dagger \hat{v}_2 - \hat{a}_i \hat{v}_2^\dagger\right) \\ &\quad + \eta \cdot \left(\hat{a}_i^\dagger \hat{a}_l + \hat{a}_l^\dagger \hat{a}_i\right) \\ &\quad + \sqrt{(1-\eta)\cdot\eta/2} \cdot \left(\hat{v}_1^\dagger \hat{a}_l + \hat{a}_l^\dagger \hat{v}_1 + \hat{v}_2^\dagger \hat{a}_l + \hat{a}_l^\dagger \hat{v}_2\right).\end{aligned} \quad (11)$$

The photon number per LO pulse is usually about $10^6 \sim 10^8$, and the photon number per signal pulse is usually about $10^0 \sim 10^1$. The value of the terms that do not include $\hat{a}_l$ is very small compared to the terms that include $\hat{a}_l$. By neglecting the small terms without $\hat{a}_l$, (11) is rewritten as

$$\begin{aligned}\hat{N}_r &= \hat{n}_{e1} - \hat{n}_{e2} = \hat{n}_1 - \hat{n}_2 \\ &= \eta \cdot |\beta| \cdot \hat{X}_{\theta_i} + \sqrt{(1-\eta)\cdot\eta/2} \cdot |\beta| \cdot \left(\hat{X}_{v1} + \hat{X}_{v2}\right),\end{aligned} \quad (12)$$

where $\hat{X}_{v1}$ and $\hat{X}_{v2}$ are the quadratures of vacuum fields $\hat{v}_1$ and $\hat{v}_2$, respectively. Combine (6) and (12), the variance of the output peak values of the TBHD is given by

$$V_{peak} = G^2 \cdot \eta |\beta|^2. \quad (13)$$

In reality, the output ratio of the 50/50 coupler may change because of the temperature fluctuations. This is equivalent to that BS_1 and BS_2 having different transmittances, which can be represented by $\eta+\varepsilon$ and $\eta-\varepsilon$, respectively (see Appendix A). Then, the photon number received by PD_1 and PD_2 are

$$\begin{aligned}\hat{n}_1 &= \hat{o}_1^\dagger \hat{o}_1 = [1-(\eta+\varepsilon)]\cdot \hat{v}_1^\dagger \hat{v}_1 \\ &+ (\eta+\varepsilon)\cdot\frac{1}{2}\left(\hat{a}_i^\dagger\hat{a}_i + \hat{a}_i^\dagger\hat{a}_l + \hat{a}_l^\dagger\hat{a}_i + \hat{a}_l^\dagger\hat{a}_l\right) \\ &+ \sqrt{[1-(\eta+\varepsilon)]\cdot(\eta+\varepsilon)/2}\left(\hat{v}_1^\dagger\hat{a}_i + \hat{v}_1^\dagger\hat{a}_l + \hat{a}_l^\dagger\hat{v}_1 + \hat{a}_i^\dagger\hat{v}_1\right),\end{aligned} \tag{14}$$

$$\begin{aligned}\hat{n}_2 &= \hat{o}_2^\dagger \hat{o}_2 = [1-(\eta-\varepsilon)]\cdot \hat{v}_2^\dagger \hat{v}_2 \\ &+ (\eta-\varepsilon)\cdot\frac{1}{2}\left(\hat{a}_i^\dagger\hat{a}_i - \hat{a}_i^\dagger\hat{a}_l - \hat{a}_l^\dagger\hat{a}_i + \hat{a}_l^\dagger\hat{a}_l\right) \\ &+ \sqrt{[1-(\eta-\varepsilon)]\cdot(\eta-\varepsilon)/2}\left(\hat{v}_2^\dagger\hat{a}_i - \hat{v}_2^\dagger\hat{a}_l - \hat{a}_l^\dagger\hat{v}_2 + \hat{a}_i^\dagger\hat{v}_2\right).\end{aligned} \tag{15}$$

The number of subtracted photoelectrons $\hat{N}_r$ is given by

$$\begin{aligned}\hat{N}_r &= \hat{n}_{e1} - \hat{n}_{e2} = \hat{n}_1 - \hat{n}_2 = \eta\cdot\left(\hat{a}_i^\dagger\hat{a}_l + \hat{a}_l^\dagger\hat{a}_i\right) \\ &+ \varepsilon\left(\hat{a}_i^\dagger\hat{a}_i + \hat{a}_l^\dagger\hat{a}_l\right) \\ &+ \sqrt{[1-(\eta+\varepsilon)]\cdot(\eta+\varepsilon)/2}\left(\hat{v}_1^\dagger\hat{a}_l + \hat{a}_l^\dagger\hat{v}_1\right) \\ &- \sqrt{[1-(\eta-\varepsilon)]\cdot(\eta-\varepsilon)/2}\left(-\hat{v}_2^\dagger\hat{a}_l - \hat{a}_l^\dagger\hat{v}_2\right).\end{aligned} \tag{16}$$

The terms $\hat{v}_1^\dagger\hat{v}_1, \hat{v}_2^\dagger\hat{v}_2, \hat{v}_1^\dagger\hat{a}_i, \hat{a}_i^\dagger\hat{v}_1, \hat{v}_2^\dagger\hat{a}_i, \hat{a}_i^\dagger\hat{v}_2$, and $\hat{a}_i^\dagger\hat{a}_i$ that don't include $\hat{a}_l$ can be neglected. The term $\eta\cdot(\hat{a}_i^\dagger\hat{a}_l + \hat{a}_l^\dagger\hat{a}_i)$ can be simplified as

$$\eta\cdot|\beta|\cdot\hat{X}_{\theta_i}. \tag{17}$$

The term $\varepsilon\hat{a}_l^\dagger\hat{a}_l$ can be transformed by using $\hat{a}_l = \beta + \delta\hat{a}_l$

$$\begin{aligned}\varepsilon\hat{a}_l^\dagger\hat{a}_l &= \varepsilon\left(|\beta|^2 + |\beta|\cdot\delta\hat{X}_l + \delta\hat{a}_l^\dagger\delta\hat{a}_l\right) \\ &= \varepsilon\left[|\beta|^2 + |\beta|\cdot\left(\delta\hat{a}_l^\dagger e^{i\theta} + \delta\hat{a}_l e^{-i\theta}\right) + \delta\hat{a}_l^\dagger\delta\hat{a}_l\right] \\ &= \varepsilon\left(|\beta|^2 + |\beta|\cdot\delta\hat{X}_l + \delta\hat{a}_l^\dagger\delta\hat{a}_l\right).\end{aligned} \tag{18}$$

The term ε has a value range from 10^{-3} to 10^{-4}, and $|\beta|^2$ has a value range from 10^6 to 10^8. Thus, the term $\varepsilon\cdot\delta\hat{a}_l^\dagger\delta\hat{a}_l$ can be neglected. The term

$$\sqrt{[1-(\eta\pm\varepsilon)]\cdot(\eta\pm\varepsilon)/2} \tag{19}$$

can be simplified as

$$\sqrt{(1-\eta)\cdot\eta/2}\cdot\left(1\pm\varepsilon\frac{(1-2\eta)}{2(1-\eta)\eta}\right), \tag{20}$$

where η is 0.6 to 0.8 for a fiber-based TBHD. Thus, the term $\varepsilon(1-2\eta)/((1-\eta)\eta)$ can be neglected. The number of subtracted photoelectrons $\hat{N}_r$ can be simplified to

$$\begin{aligned}\hat{N}_r &= \hat{n}_{e1} - \hat{n}_{e2} = \hat{n}_1 - \hat{n}_2 = \eta\cdot|\beta|\cdot\hat{X}_{\theta_i} + \varepsilon|\beta|^2 \\ &+ \sqrt{(1-\eta)\cdot\eta/2}\cdot|\beta|\cdot\left(\hat{X}_{v1} + \hat{X}_{v2}\right) + \varepsilon\cdot|\beta|\cdot\delta\hat{X}_l.\end{aligned} \tag{21}$$

At this stage, we have

$$V_{peak} = G^2\cdot\eta|\beta|^2 + G^2\cdot(\varepsilon|\beta|)^2\cdot\left(\delta\hat{X}_l\right)^2. \tag{22}$$

Eq. (22) shows that an imbalance between the two beams will introduce the remaining intensity noise $G^2\cdot(\varepsilon|\beta|)^2\cdot(\delta\hat{X}_l)^2$. The term $(\delta\hat{X}_l)^2$ represents the intensity noise of the LO pulse and usually has a value greater than 1 at low frequencies. In experiments, the displacement term $\varepsilon|\beta|^2$ does not vary with the phase θ. Thus, it can be measured and used to balance the two paths with auto-balancing technique [53]. For a TBHD, the balance or CMRR of the two paths not only depends on the intensity of the two paths but also affected by the response characteristics of the two photodiodes.

In a CVQKD system, the transmission efficiencies of signal and LO beams from the input port of the receiver to the input port of the TBHD are η_s and η_o respectively, which are modeled by $\mathrm{BS_s}$ and $\mathrm{BS_o}$ in Fig. 1. The transmission efficiency of the quantum channel is η_{ch} (modeled by $\mathrm{BS_{ch}}$). This model is suitable for a CVQKD system with or without a LO beam transmitting together with the signal beam [55]. Similar to the derivation method described above, the subtracted photoelectrons N_r can be derived as follows

$$\begin{aligned}N_r &= \eta\sqrt{\eta_{\mathrm{ch}}\eta_o\eta_s}\cdot|\gamma|\cdot\hat{X}_s + \eta\sqrt{(1-\eta_{\mathrm{ch}})\,\eta_o\eta_s}\cdot|\gamma|\cdot\hat{X}_{ch} \\ &+ \eta\sqrt{(1-\eta_s)\,\eta_o}\cdot|\gamma|\cdot\hat{X}_{vs} \\ &+ \sqrt{(1-\eta)\cdot\eta\eta_o/2}\cdot|\gamma|\cdot\left(\hat{X}_{v1} + \hat{X}_{v2}\right),\end{aligned} \tag{23}$$

where $\hat{X}_s$ is the quadrature of the signal beam $\hat{a}_s$. $\hat{X}_{ch}$ and $\hat{X}_{vs}$ are the quadratures of the vacuum fields $\hat{v}_{ch}$ and $\hat{v}_s$. $|\gamma|$ is the amplitude of the LO beam at the input port of the receiver. When the signal beam $\hat{a}_s$ is in vacuum, the variance V_{peak} becomes

$$V_{peak} = G^2\cdot\eta\eta_o|\gamma|^2 = G^2\cdot\eta|\beta|^2, \tag{24}$$

(24) shows that V_{peak} has a linear relationship with the photoelectron number per pulse $\eta|\beta|^2$ and that it has no relationship with the losses of the signal beam.

III. Calibration of the Shot Noise

When a TBHD is shot-noise-limited, it should have a linear gain G and its output quadrature values are independent [39]. The traditional method of measuring the linear gain G of TBHD is based on (24). However, this method may be affected by the intensity noise of the LO and the limited CMRR as shown in Section II. To accurately calibrate the TBHD, three gain measurement methods are presented in this section. By introducing high pass filter and comparing the fitting gain lines, the shot noise limited attribute can be accurately calibrated.

Fig. 2(a) shows a fiber-based TBHD. The signal and LO beams were injected into a 2×2 polarization-maintaining 50/50 fiber coupler, whose two output ports were connected to two photodiodes. A VOA based on bending the tail fiber of the coupler was utilized to balance the TBHD [53]. The subtracted photoelectrons from the two photodiodes are amplified by a low noise charge amplifier. Then, a shaping amplifier was used to amplify and reshape the output pulses to a Gaussian shape.

The linear gain G is determined by the charge amplifier and shaping amplifier, which can be measured directly using the electronic method as shown in Fig. 2(b). A pulse generator

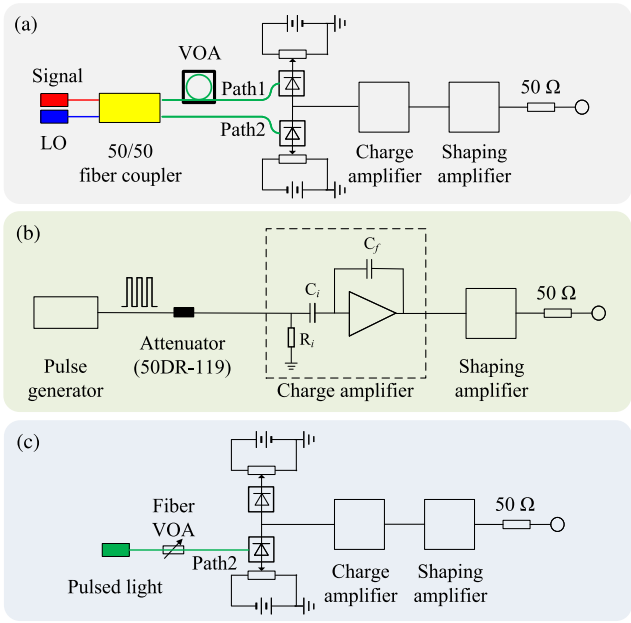

Fig. 2. The experimental setups of the shot-noise calibration for TBHD. (a) Test of the gain G_m of fiber-based TBHD. (b) Test of the gain G_e via electronic method. (c) Test of the gain G_p via integral photodetector.

generated electronic square-pulsed voltage signals with pulse width of 1 μs and pulse repetition frequency of 500 kHz. The electronic signals were attenuated by a precision attenuator (50DR-119). Then the attenuated voltage signals with amplitude U_i were guided into electronic amplifiers. The input resistor R_i had a resistance of $5\,\mathrm{M}\Omega$, and the input capacitor C_i had a capacitance of about 100 pF. The input electron number per electronic pulse N_{ele} could be calculated by

$$U_i \cdot C_i = Q_i = N_{ele} \cdot e, \tag{25}$$

where Q_i is the quantity of electric charge per electronic pulse, and e is the electric charge of one electron. By varying the input voltage U_i (N_{ele}), the output peak voltage value U_e varied accordingly as shown in Fig. 3(a). Do a linear fitting to the experimental data, a fitting black solid line GE was obtained. Its slope is the measured gain. To discriminate the real gain G and the measured gain, the measured gain is noted G_e. In experiment, the measured gain was $G_e = 7.3 \times 10^{-6}$ V/electron. The sum of residual squares for the linear fitting was $6.10 \times 10^{-29}\mathrm{V}^2$, which indicates that the amplifiers had good linearity. The relationship between U_e and N_{ele} can be expressed by

$$U_e = G_e \cdot N_{ele}. \tag{26}$$

When one photodiode of the TBHD is blocked, it becomes an integral photodetector as shown in Fig. 2(c). A 1550.4 nm pulsed laser with a repetition rate of 500 kHz and pulse width of 100 ns, followed by a fiber VOA, was directed into the photodiode PD_2 on path 2. The photon number per optical pulse N_i was tuned from 3×10^4 to 2×10^5. Fig. 3(b) shows relationship between the measured output peak voltage value U_p versus the photoelectron number per pulse N_{phe}, which is the effective photon number per optical pulse $\eta_{PD2} N_i$. The quantum efficiency of the photodiode was calibrated to $\eta_{PD2} = 80.2\%$. From the slope of the fitting line GP, the gain is determined to $G_p = 7.21 \times 10^{-6}$ V/photoelectron. The sum of residual squares for the fitting was 4.55×10^{-4} V^2. The integral photodetector exhibited good linearity

$$U_p = G_p \cdot \eta_{PD2} \cdot N_i = G_p \cdot N_{phe}. \tag{27}$$

It should be noted that the measured peak values U_e and U_p of output voltage pulses contain the electronic noise. They are measured by averaging many peak values, so various fluctuations of noise will be eliminated. The gains G_e and G_p showed only slight differences, which can mainly be attributed to a $\pm 5\%$ deviation in the capacitor C_i. Thus the measured gain G_p is more accurate than G_e, and fitting line GP can be seen as the safe line.

For the TBHD, only LO port was injected by 1550.4 nm pulsed laser. A CMRR of 76 dB was achieved by selecting matched photodiodes. The output pulsed voltage had a repetition rate of 500 kHz and full width of about 400 ns. Fig. 4(a) shows the time traces of the output pulsed voltage. The photoelectron number per pulse is 10^7, and the signal to noise ratio is $\mathrm{SNR} = 10\log_{10}(V_m/V_{ele} - 1) = 11.5\,\mathrm{dB}$. Here V_m is the variance of the measured peak voltage value U_m, and V_{ele} is the electronics variance. Fig. 4(b) shows the various noise variances versus photon number per LO pulse $|\beta|^2$. The black squares represents the variance V_m. The red circles represent the variance V_{ele}. The green triangles represent the measured variance V^m_{peak}, which can be obtained by

$$V^m_{peak} = V_m - V_{ele} = G_m^2 \cdot \eta \cdot |\beta|^2. \tag{28}$$

Finding the square roots of both sides of (28) results in

$$\sqrt{V^m_{peak}} = G_m \cdot \sqrt{\eta \cdot |\beta|^2}. \tag{29}$$

Fig. 3(c) plots the squared data of the green triangle points in Fig. 4(b). The title of horizontal coordinate of Fig. 3(c) is square root of photoelectron number per LO pulse $\sqrt{\eta \cdot |\beta|^2}$, and the title of longitudinal coordinate is standard variance of V^m_{peak} or $\sqrt{V^m_{peak}}$. From the slope of the fitting line GM, the gain is determined to $G_m = 7.16 \times 10^{-6}$ V/particle. The sum of residual squares for the fitting was 7.63×10^{-8} V^2. Fig. 3(d) shows that the fitting gain lines GM and GP nearly overlapped with an error about $\pm 1‰$ in the experiment, a stable low-loss fiber connector and suitable high-pass filter were used to minimize the measurement error. Fig. 4(c) shows the whole spectra of TBHD when a continuous 1550.4 nm laser beam was injected into the LO port. Fig. 4(d) and (e) plot the spectra at low frequency when one and three orders high-pass filter were used respectively. Due to the low frequency intensity noise of the pulsed LO and limited CMRR, the gain G_m is usually higher than the gain G_p. When the low frequency intensity noise decreases, the gain G_m will approach the gain G_p. In the calibration process, the gain G_m of the TBHD using one-order high-pass filter at low frequency is 5% – 6% higher than the gain G_p. By using the three-order high-pass filter the fitting line GM is well overlapped with fitting line GP with error about 1‰.

The experiment results of Fig. 3 demonstrate that the improved TBHD has a good linear gain G. To further ensure that the

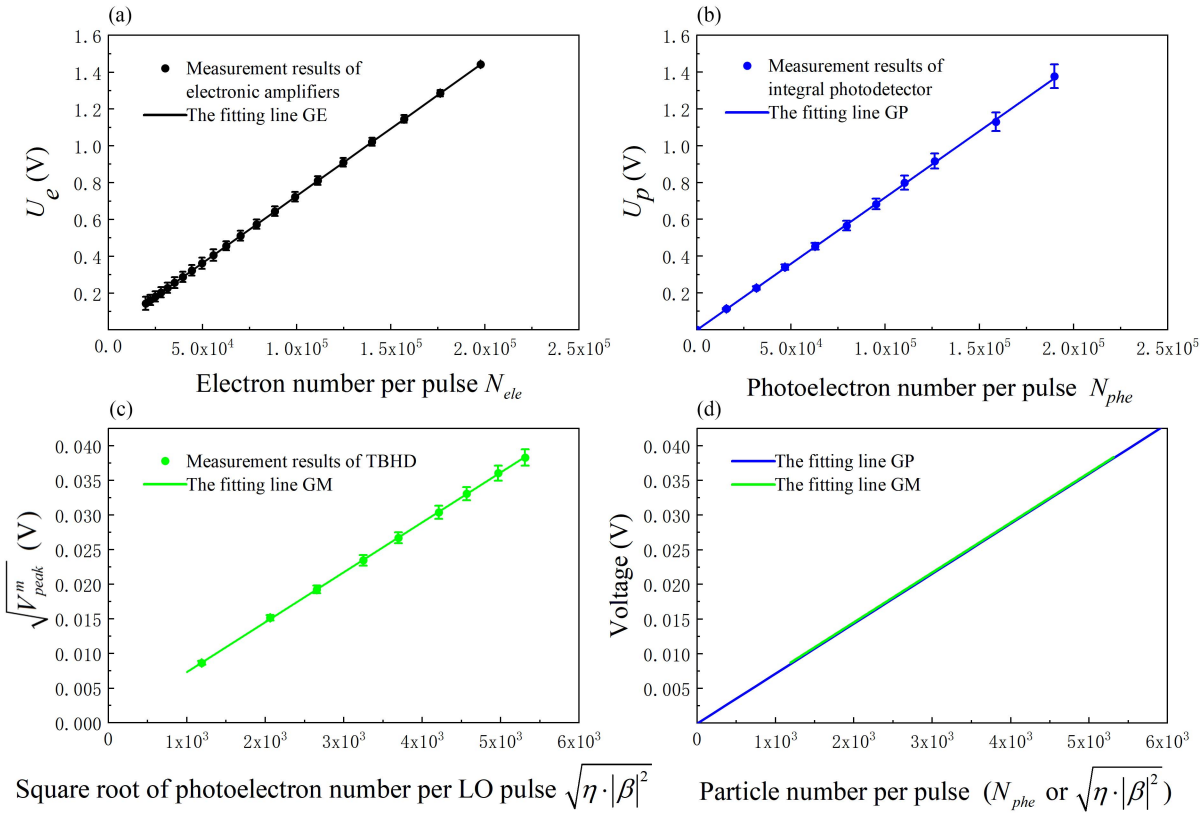

Fig. 3. Linear performance of the electronic amplifiers, integral photodetector and TBHD. (a) Measurement results of the electronic amplifiers and the fitting line GE. (b) Measurement results of the integral photodetector and the fitting line GP. (c) Measurement results of the TBHD and the fitting line GM. (d) Comparison of the fitting lines GP and GM.

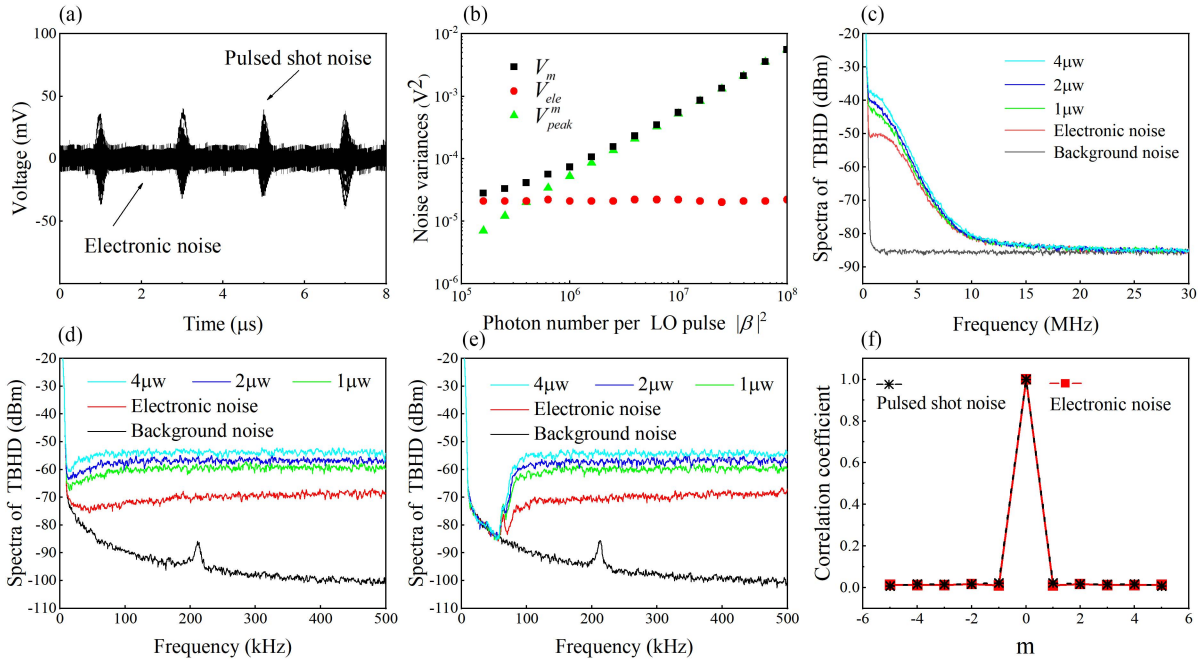

Fig. 4. Characteristics of the TBHD. (a) Time traces of the output pulsed noise for vacuum field input. (b) Various noise variances versus the photon number per LO pulse. (c) The whole spectra of the TBHD with continuous laser input. (d) Low-frequency part of (c) with one-order high-pass filter. (e) Low-frequency part of (c) with three-order high-pass filter. (f) The correlation coefficients of measured peak voltage values of pulsed shot noise and electronic noise.

TBHD is indeed shot noise limited, the output peak voltage values should be independent. To ensure the measured peak voltage values or the corresponding quadratures are independent [39], we investigated the correlation coefficients between adjacent values. A sequence of measured peak voltage values denoted by $X_i(i = 1, 2, \ldots, n)$ were used. The correlation coefficient $CC(m)$ can be calculated as

$$CC(m) = \frac{E\left(X_i \cdot X_{i+m}\right) - E\left(X_i\right) \cdot E\left(X_{i+m}\right)}{\sqrt{E\left(X_i^2\right) - E^2\left(X_i\right)} \cdot \sqrt{E\left(X_{i+m}^2\right) - E^2\left(X_{i+m}\right)}}, \tag{30}$$

where $E(X)$ represents the expectation value of X [51]. The value of n is 10^5, and m takes the value between -5 and 5. The calculation results are shown in Fig. 4(f). The black star points represent the correlation coefficients of the measured peak voltage values of pulsed shot noise at $\mathrm{SNR} = 11.5\,\mathrm{dB}$, and the red square points represent the correlation coefficients of electronic noise. We can see clearly that a complete correlation occurs when $m = 0$, whereas the correlation vanishes for $m \neq 0$. Then we can conclude that measured peak voltage values (corresponding to the quadratures of vacuum field) are independent and the TBHD is surely shot noise limited.

IV. The Security Analysis of CVQKD System Due to Inaccurate Shot Noise Calibration

In the CVQKD systems, various types of variances are normalized to the shot noise variance. If the shot noise cannot be calibrated accurately, security loopholes may be generated.

In CVQKD experiments, the measured variance V_{peak}^m can be obtained using (28).

$$\begin{aligned} V_{peak}^m &= V_m - V_{ele} \\ &= (V_B - V_e) \cdot \eta |\beta|^2 G^2 = (V_B - V_e) \cdot V_0, \end{aligned} \tag{31}$$

where V_m is the total variance measured at the receiver side and V_{ele} is the electronic noise. V_B and V_e are the corresponding normalized values. V_0 represents the shot noise variance with the real gain G. The variance of the signal beam is given by

$$V = V_A + 1, \tag{32}$$

where V_A is the normalized modulation variance and the value of 1 represents the shot noise variance. They are both the normalized values. Based on (23), (31) can be rewritten as

$$(V_B - V_e) \cdot V_0 = \left[\eta_{ch}\eta_s\eta\left(V_A + \xi\right) + 1\right] \cdot V_0, \tag{33}$$

where ξ is the excess noise of the CVQKD system. We use the calibrated gain G_p and the corresponding shot noise V_0^p to normalize the measure variance. In this case, (33) becomes

$$(V_B - V_e) \cdot \frac{V_0}{V_0^p} = \left[\eta_{ch}\eta_s\eta\left(V_A + \xi\right) + 1\right] \cdot \frac{V_0}{V_0^p}. \tag{34}$$

V_B and V_e are calibrated as $V_B^p = V_B V_0 / V_0^p$ and $V_e^p = V_e V_0 / V_0^p$ respectively, and the transmission efficiency is calculated as $\eta_{ch}^p = \eta_{ch} V_0 / V_0^p$. The estimated excess noise will be

$$\xi^p = \xi + \frac{1}{\eta_{ch}^p \eta_s \eta}\left(\frac{V_0}{V_0^p} - 1\right). \tag{35}$$

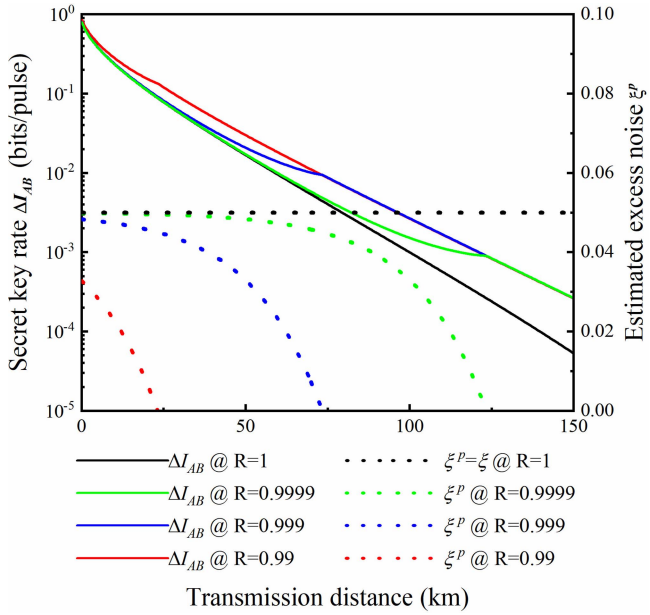

Fig. 5. Estimated excess noise and secret key rate versus the transmission distance for V_0/V_0^p less than 1. The parameters of the CVQKD system are $\xi = 0.05$, $\eta = 0.8$, $\eta_s = 0.74$, $\beta = 0.98$, $V_A = 10$, and $V_e = 0.1$.

Then, (34) can be rewritten as

$$V_B^p - V_e^p = \eta_{ch}^p \eta_s \eta \left(V_A + \xi^p\right) + 1. \tag{36}$$

When $G_p > G$ or $V_0^p > V_0$, the estimated excess noise ξ^p is less than the real excess noise ξ. The values of the other parameters used to calculate the secret key rate also change. The secret key rate under collective attack is given by [32]

$$\Delta I_{AB} = \beta \cdot I_{AB} - \chi_{BE}, \tag{37}$$

where ΔI_{AB} is the secret key rate, I_{AB} is the Shannon mutual information between Alice and Bob, χ_{BE} is the von Neumann information eavesdropped by Eve, and β is the reconciliaiton efficiency. Fig. 5 shows the estimated excess noise and secret key rate versus the transmission distance at different ratios $R = V_0/V_0^p$ under collective attack. The green, blue, and red dotted lines represent the estimated excess noise ξ^p at ratios of 0.9999, 0.999, and 0.99 respectively. When the calibrated value G_p or V_0^p is larger, the ratio is smaller, and the estimated excess noise ξ^p decreases more rapidly with the distance. The decreasing of estimated excess noise ξ^p will lead to overestimation of the secret key rate, as indicated by the green, blue, and red solid lines. The black solid line represents the secret key rate when the shot noise is calibrated accurately $(R = 1)$. When the estimated excess noises ξ^p decrease to zero or less than zero, it is set to zero. This will lead to the changing of the secret key rate trend. The black dot line represents the real excess noise $\xi = 0.05$ of the CVQKD system. By comparing the red, blue and green solid lines with the black solid line, we can see that when $G_p > G$, the calculated secret key rate will be overestimated. It means that loophole is generated.

When $G_p < G$ or $V_0^p < V_0$, the estimated excess noise ξ^p is greater than the real excess noise ξ. Fig. 6 presents the estimated excess noise and secret key rate versus the transmission distance

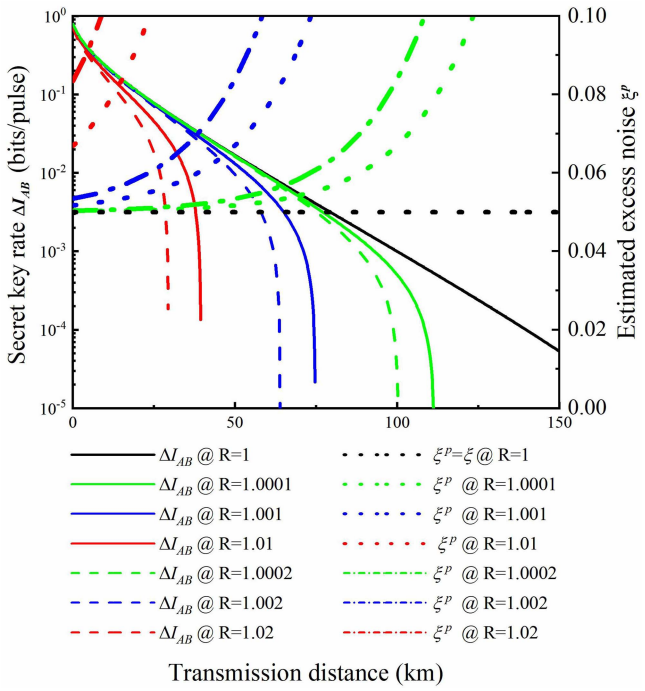

Fig. 6. Estimated excess noise and secret key rate versus the transmission distance at ratios greater than 1.

at different ratios $R = V_0/V_0^p$ under collective attack. The green, blue, and red dotted lines represent the estimated excess noise ξ^p at ratios of 1.0001, 1.001, and 1.01, respectively. The black dotted line represents the real excess noise of the CVQKD system. When the calibrated value G_p or V_0^p is smaller, the ratio is larger, and the estimated excess noise ξ^p increases more rapidly with the distance. Correspondingly, the secret key rate decreases more rapidly, as shown by the green, blue, and red solid lines. By comparing the red, blue and green solid lines with the black solid line in Fig. 6, we can see that when $G_p < G$, the calculated secret key rate will be underestimated, which degrade the performance of the CVQKD.

In the CVQKD systems, the laser and modulators used to generate LO pulses may be disturbed by the electromagnetic interference or other factors, and the LO pulses in the transmission channel may be attacked by Eavesdropper. Then, the intensity noise of the LO pulses will become larger, and it may exist in all the frequency band of the TBHD. In this case, the noise V_0^m of the LO pulses will be greater than V_0. Eq. (33) becomes

$$(V_B - V_e) \cdot V_0^m = [\eta_{ch}\eta_s\eta\,(V_A + \xi) + 1] \cdot V_0^m. \tag{38}$$

When the gain $G_p = G$ is used to normalize the measured variance, (38) is transformed to

$$(V_B - V_e) \cdot \frac{V_0^m}{V_0^p} = [\eta_{ch}\eta_s\eta\,(V_A + \xi) + 1] \cdot \frac{V_0^m}{V_0^p}. \tag{39}$$

Here, the the estimated excess noise ξ^p and secret key rate versus the transmission distance are the same as the results shown by the dotted and solid lines in Fig. 6 at the ratios 1.0001, 1.001, and 1.01. However, the meaning is different. When the gain $G_p = G$, intensity noise of the LO pulse will degrades the performance of CVQKD. However, no loophole is generated. In paper [56], there is no safe line GP or V_0^p to normalize the variance, the intensity noise of LO pulse will generate loopholes.

Notice that, measurement errors during calibration of the TBHD are usually inevitable. To avoid security loopholes caused by a high gain G_p, we can decrease the slope of the safe line GP or gain G_p. The decreased gain is noted as G^d, and the corresponding shot noise is represented by V_0^d. Eq. (33) becomes

$$(V_B - V_e) \cdot \frac{V_0}{V_0^d} = [\eta_{ch}\eta_s\eta\,(V_A + \xi) + 1] \cdot \frac{V_0}{V_0^d}. \tag{40}$$

In this situation, the estimated excess noise ξ^p and secret key rate versus the transmission distance are the same as the results shown by the dotted and solid lines in Fig. 6 at the ratios 1.0001, 1.001, and 1.01. It means that the security loopholes can be closed at the cost of sacrificing the secret key rate if we decrease the calibrated gain in advance.

If the measured noise V_0^m of the LO pulse is greater than the shot noise V_0 at the ratios $R = V_0^m/V_0$ of 1.0001, 1.001, and 1.01. And the noise V_0^d is decreased at ratios $R = V_0/V_0^d$ of 0.9999, 0.999, and 0.99 respectively. Then the normalized expression is

$$(V_B - V_e) \cdot \frac{V_0^m}{V_0^d} = [\eta_{ch}\eta_s\eta\,(V_A + \xi) + 1] \cdot \frac{V_0^m}{V_0^d}. \tag{41}$$

Then the estimated excess noise ξ^p and secret key rate versus the transmission distance are represented by the dot-dash and dash lines in Fig. 6 at the ratios $R = V_0^m/V_0^d$ of 1.0002, 1.002, and 1.02. It means at the situation of LO pulse with higher intensity noise V_0^m and decreased shot noise V_0^d, the secret key rate will be underestimated. It should be noted that no loophole is generated. We can see that the method of decreasing the slope of safe line can be used to ensure that noise V_0^m will not generate loopholes but only reduce the performance of the CVQKD system.

The above results show that the secret key rate is very sensitive to the shot noise calibration. Calibrating the shot-noise-limited attribute of TBHD with high accuracy is critical for ensuring the safety of CVQKD systems. By decreasing the calibrated gain of the TBHD, we can effectively avoid the security loopholes due to the measurement error during the shot-noise calibration.

V. Conclusion

In this study, an accurate model and method for calibrating the shot-noise-limited attribute of a TBHD were established. The proposed method involves overlapping the gain lines of the integral photodetector and TBHD to calibrate the shot-noise-limited attribute. The gain line measured by the integral photodetector can eliminate the effect of various noises. To eliminate the influence of remaining intensity noise at low frequencies, a high-order high-pass filter is utilized. In experiments, a measurement error of about ±1‰ was achieved. The effect of measurement error on the security of the CVQKD system was analyzed, and a countermeasure was proposed to avoid security loopholes. The proposed methods can be applied to CVQKD systems with or without LO beam transmitting together with the signal beam,

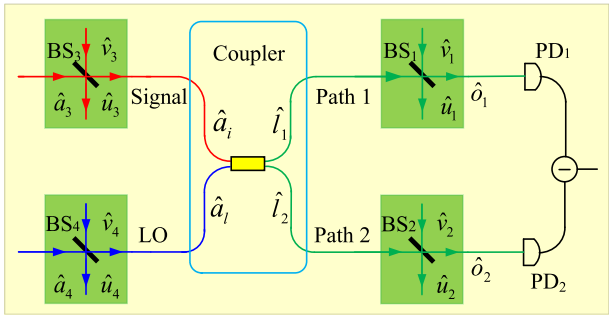

Fig. 7. Model of a realistic 50/50 coupler.

and they are expected to contribute to the security of CVQKD systems and standardization of TBHD.

Appendix A
Realistic 50/50 Coupler Model

Fig. 7 shows the model of a realistic 50/50 coupler. The transmission efficiency η_i of the coupler has a deviation from 1/2. We can't sure whether the losses of realistic coupler are before or after the coupler, or both. Then, all the losses before and after the coupler are considered, and they are equivalent to BS_1, BS_2, BS_3, and BS_4 with transmission efficiencies η_1, η_2, η_3, and η_4. We assume that PD_1 and PD_2 are ideal photodiodes with 100% efficiency. The nonideal efficiencies of the photodiodes are combined into the transmission efficiencies of BS_1 and BS_2, respectively.

The signal beam $\hat{a}_i$ interferes with the LO beam $\hat{a}_l$ on the 50/50 coupler. The output beams $\hat{l}_1$ and $\hat{l}_2$ interfere with the vacuum beams $\hat{v}_1$ and $\hat{v}_2$, and output $\hat{o}_1$ and $\hat{o}_2$, respectively. Above transformations are given as follows:

$$\begin{bmatrix} \hat{l}_1 \\ \hat{l}_2 \end{bmatrix} = \begin{bmatrix} \sqrt{1-\eta_i} & \sqrt{\eta_i} \\ \sqrt{\eta_i} & -\sqrt{1-\eta_i} \end{bmatrix} \cdot \begin{bmatrix} \hat{a}_i \\ \hat{a}_l \end{bmatrix}, \tag{42}$$

$$\begin{bmatrix} \hat{o}_1 \\ \hat{u}_1 \end{bmatrix} = \begin{bmatrix} \sqrt{1-\eta_1} & \sqrt{\eta_1} \\ \sqrt{\eta_1} & -\sqrt{1-\eta_1} \end{bmatrix} \cdot \begin{bmatrix} \hat{v}_1 \\ \hat{l}_1 \end{bmatrix},$$

and

$$\begin{bmatrix} \hat{o}_2 \\ \hat{u}_2 \end{bmatrix} = \begin{bmatrix} \sqrt{1-\eta_2} & \sqrt{\eta_2} \\ \sqrt{\eta_2} & -\sqrt{1-\eta_2} \end{bmatrix} \cdot \begin{bmatrix} \hat{v}_2 \\ \hat{l}_2 \end{bmatrix}. \tag{43}$$

The number of photoelectrons $\hat{N}_1$ in PD_1 is given by

$$\begin{aligned} \hat{N}_1 = \hat{o}_1^\dagger \hat{o}_1 &= \left(\sqrt{1-\eta_1}\hat{v}_1^\dagger + \sqrt{\eta_1}\hat{l}_1^\dagger\right)\left(\sqrt{1-\eta_1}\hat{v}_1 + \sqrt{\eta_1}\hat{l}_1\right) \\ &= (1-\eta_1)\,\hat{v}_1^\dagger\hat{v}_1 \\ &\quad + \eta_1\left[(1-\eta_i)\,\hat{a}_i^\dagger\hat{a}_i + \sqrt{\eta_i\,(1-\eta_i)}\right. \\ &\quad \left.\times\left(\hat{a}_i^\dagger\hat{a}_l + \hat{a}_l^\dagger\hat{a}_i\right) + \eta_i\hat{a}_l^\dagger\hat{a}_l\right] \\ &\quad + \sqrt{(1-\eta_i)\,\eta_1\,(1-\eta_1)}\left(\hat{v}_1^\dagger\hat{a}_i + \hat{a}_i^\dagger\hat{v}_1\right) \\ &\quad + \sqrt{\eta_i\eta_1\,(1-\eta_1)}\left(\hat{v}_1^\dagger\hat{a}_l + \hat{a}_l^\dagger\hat{v}_1\right). \end{aligned} \tag{44}$$

The number of photoelectrons $\hat{N}_2$ in PD_2 is expressed by

$$\begin{aligned} \hat{N}_2 = \hat{o}_2^\dagger \hat{o}_2 &= \left(\sqrt{1-\eta_2}\hat{v}_2^\dagger + \sqrt{\eta_2}\hat{l}_2^\dagger\right)\left(\sqrt{1-\eta_2}\hat{v}_2 + \sqrt{\eta_2}\hat{l}_2\right) \\ &= (1-\eta_2)\,\hat{v}_2^\dagger\hat{v}_2 \\ &\quad + \eta_2\left[\eta_i\hat{a}_i^\dagger\hat{a}_i - \sqrt{\eta_i\,(1-\eta_i)}\left(\hat{a}_i^\dagger\hat{a}_l + \hat{a}_l^\dagger\hat{a}_i\right)\right. \\ &\quad \left.+ (1-\eta_i)\,\hat{a}_l^\dagger\hat{a}_l\right] \\ &\quad + \sqrt{\eta_i\eta_2\,(1-\eta_2)}\left(\hat{v}_2^\dagger\hat{a}_i + \hat{a}_i^\dagger\hat{v}_2\right) \\ &\quad - \sqrt{(1-\eta_i)\,\eta_2\,(1-\eta_2)}\left(\hat{v}_2^\dagger\hat{a}_l + \hat{a}_l^\dagger\hat{v}_2\right). \end{aligned} \tag{45}$$

The number of subtracted photoelectrons is given by

$$\begin{aligned} \hat{N}_r &= \hat{N}_1 - \hat{N}_2 = (\eta_1+\eta_2)\sqrt{\eta_i\,(1-\eta_i)}\left(\hat{a}_i^\dagger\hat{a}_l + \hat{a}_l^\dagger\hat{a}_i\right) \\ &\quad + \sqrt{\eta_i\eta_1\,(1-\eta_1)}\left(\hat{v}_1^\dagger\hat{a}_l + \hat{a}_l^\dagger\hat{v}_1\right) + \eta_1\eta_i\hat{a}_l^\dagger\hat{a}_l \\ &\quad + \sqrt{(1-\eta_i)\,\eta_2\,(1-\eta_2)}\left(\hat{v}_2^\dagger\hat{a}_l + \hat{a}_l^\dagger\hat{v}_2\right) - \eta_2\,(1-\eta_i)\,\hat{a}_l^\dagger\hat{a}_l \\ &= (\eta_1+\eta_2)\sqrt{\eta_i\,(1-\eta_i)}\cdot|\beta|\cdot\hat{X}_{\theta_i} \\ &\quad + \sqrt{\eta_i\eta_1\,(1-\eta_1)}\cdot|\beta|\cdot\hat{X}_{\theta_1} \\ &\quad + \sqrt{(1-\eta_i)\,\eta_2\,(1-\eta_2)}\,|\beta|\cdot\hat{X}_{\theta_2} \\ &\quad + [\eta_1\eta_i - \eta_2\,(1-\eta_i)]\,\hat{a}_l^\dagger\hat{a}_l. \end{aligned} \tag{46}$$

To derive (46), small terms have been neglected. $\hat{X}_\theta$ is the quadrature, and θ is the LO phase. To calibrate the shot-noise-limited attribute, the signal beam is a vacuum field. Then, the variance of the subtracted photoelectrons is given by

$$\begin{aligned} V_r = &\left[(\eta_1+\eta_2)^2\eta_i\,(1-\eta_i) + \eta_i\eta_1\,(1-\eta_1)\right. \\ &\left.+ (1-\eta_i)\,\eta_2\,(1-\eta_2)\right]\cdot|\beta|^2. \end{aligned} \tag{47}$$

Considering the losses of signal path and LO path, the relations of $\hat{a}_3$, $\hat{a}_4$ and $\hat{a}_i$, $\hat{a}_l$ are given by

$$\begin{bmatrix} \hat{a}_i \\ \hat{u}_3 \end{bmatrix} = \begin{bmatrix} \sqrt{1-\eta_3} & \sqrt{\eta_3} \\ \sqrt{\eta_3} & -\sqrt{1-\eta_3} \end{bmatrix} \cdot \begin{bmatrix} \hat{v}_3 \\ \hat{a}_3 \end{bmatrix},$$

$$\begin{bmatrix} \hat{a}_l \\ \hat{u}_4 \end{bmatrix} = \begin{bmatrix} \sqrt{1-\eta_4} & \sqrt{\eta_4} \\ \sqrt{\eta_4} & -\sqrt{1-\eta_4} \end{bmatrix} \cdot \begin{bmatrix} \hat{v}_4 \\ \hat{a}_4 \end{bmatrix}, \tag{48}$$

Using (48), (46) is rewritten as

$$\begin{aligned} \hat{N}_r &= \hat{N}_1 - \hat{N}_2 \\ &= (\eta_1+\eta_2)\sqrt{\eta_i\,(1-\eta_i)}\left[\sqrt{\eta_4\,(1-\eta_3)}\left(\hat{v}_3^\dagger\hat{a}_4 + \hat{v}_3\hat{a}_4^\dagger\right)\right. \\ &\quad \left.+\sqrt{\eta_4\eta_3}\left(\hat{a}_3^\dagger\hat{a}_4 + \hat{a}_3\hat{a}_4^\dagger\right)\right] + \eta_1\eta_i\hat{a}_l^\dagger\hat{a}_l - \eta_2\,(1-\eta_i)\,\hat{a}_l^\dagger\hat{a}_l \\ &\quad + \sqrt{\eta_i\eta_1\,(1-\eta_1)}\sqrt{\eta_4}\left(\hat{v}_1^\dagger\hat{a}_4 + \hat{a}_4^\dagger\hat{v}_1\right) \\ &\quad + \sqrt{(1-\eta_i)\,\eta_2\,(1-\eta_2)}\sqrt{\eta_4}\left(\hat{v}_2^\dagger\hat{a}_4 + \hat{a}_4^\dagger\hat{v}_2\right) \\ &= (\eta_1+\eta_2)\sqrt{\eta_i\,(1-\eta_i)}\,|\gamma|\left[\sqrt{\eta_4\,(1-\eta_3)}\hat{X}_{\theta_3} + \sqrt{\eta_d\eta_c}\hat{X}_{a_3}\right] \end{aligned}$$

$$+\sqrt{\eta_i\eta_1\left(1-\eta_1\right)}\sqrt{\eta_4}\left|\gamma\right|\hat{X}_{\theta_1}$$
$$+\sqrt{\left(1-\eta_i\right)\eta_2\left(1-\eta_2\right)}\sqrt{\eta_4}\left|\gamma\right|\hat{X}_{\theta_2}$$
$$+\left[\eta_1\eta_i-\eta_2\left(1-\eta_i\right)\right]\left[\sqrt{\left(1-\eta_4\right)\eta_4}\left|\gamma\right|\hat{X}_{\theta_4}+\eta_4\hat{a}_4^{\dagger}\hat{a}_4\right]. \tag{49}$$

Assume that the signal beam $\hat{a}_3$ is a vacuum field and $|\gamma|$ is the amplitude of the LO beam $\hat{a}_4$, the variance of the subtracted photoelectrons is given by

$$\begin{aligned}V_r=&\left[\left(\eta_1+\eta_2\right)^2\eta_i\left(1-\eta_i\right)+\eta_i\eta_1\left(1-\eta_1\right)\right.\\&+\left(1-\eta_i\right)\eta_2\left(1-\eta_2\right)\\&\left.+\left[\eta_1\eta_i-\eta_2\left(1-\eta_i\right)\right]^2\left(1-\eta_4\right)\right]\cdot\eta_4|\gamma|^2.\end{aligned} \tag{50}$$

A comparison between (47) and (50) shows that the transmission efficiency η_3 of the signal path has no influence on the variance V_r when the signal beam $\hat{a}_3$ is a vacuum field. The transmission efficiency η_4 affects the number of photoelectrons, with $\eta_4|\gamma|^2=|\beta|^2$. To calibrate the shot-noise-limited attribute, a VOA is inserted into one of the output paths of the coupler to ensure that the two output paths are balanced

$$\eta_i\eta_1\eta_4=\left(1-\eta_i\right)\eta_2\eta_4. \tag{51}$$

In this case, the variance of the subtracted photoelectrons is given by

$$\begin{aligned}V_r=&\left[\left(\eta_1+\eta_2\right)^2\eta_i\left(1-\eta_i\right)+\eta_i\eta_1\left(1-\eta_1\right)\right.\\&\left.+\left(1-\eta_i\right)\eta_2\left(1-\eta_2\right)\right]\cdot\left|\beta\right|^2\\=&\,2\eta_i\eta_1\left|\beta\right|^2\\=&\,2\left(1-\eta_i\right)\eta_2\left|\beta\right|^2,\end{aligned} \tag{52}$$

where $2\eta_i\eta_1|\beta|^2$ or $2(1-\eta_i)\eta_2|\beta|^2$ is the number of photoelectrons of the two photodiodes. The efficiency η_i has a small deviation from 1/2 that can be written as $\eta_i=1/2\pm\delta$. Before balancing the TBHD, suppose that $\eta_i\eta_1=(1/2\pm\delta)\eta_1$ is greater than $(1-\eta_i)\eta_2=(1/2\mp\delta)\eta_2$. The transmission efficiency η_1 can be decreased by the a VOA to balance the two output paths.

For the model in Fig. 1, when the two output paths are balanced, the transmission efficiency of either path 1 or path 2 is

$$2\eta_i\eta_1\eta_4=2\left(1-\eta_i\right)\eta_2\eta_4. \tag{53}$$

The two models have the same number of photoelectrons. We can see that all the losses in the model of Fig. 7 can be placed after the coupler in the model of Fig. 1. Thus, the two models are equivalent when the two output paths are balanced. The transmission efficiency of path 2 without the VOA can be used to calibrate the total transmission efficiency. The transmission efficiency η_i may change due to the environmental temperature. If the transmission efficiency changes slightly, η_i becomes $\eta_i=1/2\pm\delta\pm\Delta$, and $1-\eta_i$ becomes $1-\eta_i=1/2\mp\delta\mp\Delta$. For path 1, the transmission efficiency changes $\pm\Delta\cdot\eta_1$; for path 2, the transmission efficiency changes $\mp\Delta\cdot\eta_2$. Because Δ is a small value, the difference between η_1 and η_2 is very small, the approximation $\Delta\cdot\eta_1\approx\Delta\cdot\eta_2$ represented by ε can be used. When the VOA is used to rebalance the two paths, the efficiency of the calibration path is changed from $(1/2\mp\delta)\eta_2$ to $(1/2\mp\delta\mp\Delta)\eta_2$. This will introduce a measurement error during the calibration process.

REFERENCES

[1] H.-P. Yuen and V.-W.-S. Chan, "Noise in homodyne and heterodyne detection," *Opt. Lett.*, Vol. 8, no. 3, pp. 177–179, Mar. 1983.

[2] S.-L. Braunstein and P.-V. Loock, "Quantum information with continuous variables," *Rev. Mod. Phys.*, Vol. 77, no. 2, pp. 513–577, Jun. 2005.

[3] R.-E. Slusher, L.-W. Hollberg, B. Yurke, J.-C. Mertz, and J.-F. Valley, "Observation of squeezed states generated by four-wave mixing in an optical cavity," *Phys. Rev. Lett.*, Vol. 55, no. 22, pp. 2409–2412, Nov. 1985.

[4] L.-A. Wu, H.-J. Kimble, J.-L. Hall, and H. Wu, "Generation of squeezed states by parametric down conversion," *Phys. Rev. Lett.*, vol. 57, no. 20, pp. 2520–2523, Nov. 1986.

[5] H. Vahlbruch, M. Mehmet, K. Danzmann, and R. Schnabel, "Detection of 15 dB squeezed states of light and their application for the absolute calibration of photoelectric quantum efficiency," *Phys. Rev. Lett.*, Vol. 117, no. 11, Sep. 2016, Art. no. 110801.

[6] U.-L. Andersen, T. Gehring, C. Marquardt, and G. Leuchs, "30 years of squeezed light generation," *Phys. Scripta*, vol. 91, no. 5, Apr. 2016, Art. no. 053001.

[7] S.-P. Shi, L. Tian, Y.-J. Wang, Y.-H. Zheng, C.-D. Xie, and K.-C. Peng, "Demonstration of channel multiplexing quantum communication exploiting entangled sideband modes," *Phys. Rev. Lett.*, vol. 125, no. 7, Aug. 2020, Art. no. 070502.

[8] X.-M. Guo, C.-D. Xie, and Y.-M. Li, "Generation and homodyne detection of continuous-variable entangled optical beams with a large wavelength difference," *Phys. Rev. A*, vol. 84, no. 2, Aug. 2011, Art. no. 020301.

[9] Z.-Y. Ou, S.-F. Pereira, H.-J. Kimble, and K.-C. Peng, "Realization of the Einstein-Podolsky-Rosen paradox for continuous variables," *Phys. Rev. Lett.*, vol. 68, no. 25, pp. 3663–3666, Jun. 1992.

[10] S.-L. Braunstein and H.-J. Kimble, "Teleportation of continuous quantum variables," *Phys. Rev. Lett.*, vol. 80, no. 4, pp. 869–872, Jan. 1998.

[11] A. Furusawa, J.-L. Sorensen, S.-L. Braunstein, C.-A. Fuchs, H.-J. Kimble, and E.-S. Polzik, "Unconditional quantum teleportation," *Science*, vol. 282, no. 5389, pp. 706–709, Oct. 1998.

[12] M.-R. Huo et al., "Deterministic quantum teleportation through fiber channels," *Sci. Adv.*, vol. 4, no. 10, Oct. 2018, Art. no. 9401.

[13] I. Kogias, A.-R. Lee, S. Ragy, and G. Adesso, "Quantification of Gaussian quantum steering," *Phys. Rev. Lett.*, vol. 114, no. 6, Feb. 2015, Art. no. 060403.

[14] R. Uola, A.-C.-S. Costa, H.-C. Nguyen, and O. Gühne, "Quantum steering," *Rev. Mod. Phys.*, vol. 92, no. 1, Mar. 2020, Art. no. 015001.

[15] Y. Liu et al., "Distillation of Gaussian Einstein-Podolsky-Rosen steering with noiseless linear amplification," *npj Quantum Inf.*, vol. 8, no. 38, Apr. 2022, Art. no. 060403.

[16] C. Gabriel et al., "A generator for unique quantum random numbers based on vacuum states," *Nature Photon.*, vol. 4, no. 10, pp. 711–715, Aug. 2010.

[17] Y. Shen, L. Tian, and H. Zou, "Practical quantum random number generator based on measuring the shot noise of vacuum states," *Phys. Rev. A*, vol. 81, no. 6, Jun. 2010, Art. no. 063814.

[18] T. Symul, S.-M. Assad, and P.-K. Lam, "Real time demonstration of high bitrate quantum random number generation with coherent laser light," *Appl. Phys. Lett.*, vol. 98, no. 23, Jun. 2011, Art. no. 231103.

[19] X.-F. Ma, X. Yuan, Z. Cao, B. Qi, and Z. Zhang, "Quantum random number generation," *npj Quantum Inf.*, vol. 2, Jun. 2016, Art. no. 16021.

[20] Z.-G. Lu, J.-Q. Liu, X.-Y. Wang, P. Wang, Y.-M. Li, and K.-C. Peng, "Quantum random number generator with discarding-boundary-bin measurement and multi-interval sampling," *Opt. Exp.*, vol. 29, no. 8, pp. 12440–12453, Apr. 2021.

[21] A.-I. Lvovsky and M.-G. Raymer, "Continuous-variable optical quantum-state tomography," *Rev. Mod. Phys.*, vol. 81, no. 1, pp. 299–332, Mar. 2009.

[22] N.-J. Cerf, M. Levy, and G.-V. Assche, "Quantum distribution of Gaussian keys using squeezed states," *Phys. Rev. A*, vol. 63, no. 5, May 2001, Art. no. 052311.

[23] A.-M. Lance et al., "No-switching quantum key distribution using broadband modulated coherent light," *Phys. Rev. Lett.*, vol. 95, no. 18, Oct. 2005, Art. no. 180503.
[24] N. Wang, S.-N. Du, W.-Y. Liu, X.-Y. Wang, Y.-M. Li, and K.-C. Peng, "Long-distance continuous-variable quantum key distribution with entangled states," *Phys. Rev. Appl.*, vol. 10, no. 6, Dec. 2018, Art. no. 064028.
[25] C. Weedbrook, S. Pirandola, R. García-Patrón, N.-J. Cerf, and T.-C. Ralph, "Gaussian quantum information," *Rev. Mod. Phys.*, vol. 84, no. 2, pp. 621–669, Jun. 2012.
[26] D.-T. Smithey, M. Beck, M.-G. Raymer, and A. Faridani, "Measurement of the Wigner distribution and the density matrix of a light mode using optical homodyne tomography: Application to squeezed states and the vacuum," *Phys. Rev. Lett.*, vol. 70, no. 9, pp. 1244–1247, Mar. 1993.
[27] G. Breitenbach, S. Schiller, and J. Mlynek, "Measurement of the quantum states of squeezed light," *Nature*, vol. 387, pp. 471–475, May 1997.
[28] M. Vasilyev, S.-K. Choi, P. Kumar, and G.-M. D'Ariano, "Tomographic measurement of joint photon statistics of the twin-beam quantum state," *Phys. Rev. Lett.*, vol. 84, no. 11, pp. 2354–2357, Mar. 2000.
[29] F. Grosshans and P. Grangier, "Continuous variable quantum cryptography using coherent states," *Phys. Rev. Lett.*, vol. 88, no. 5, Feb. 2002, Art. no. 057902.
[30] C. Silberhorn, T.-C. Ralph, N. Lutkenhaus, and G. Leuchs, "Continuous variable quantum cryptography: Beating the 3 dB loss limit," *Phys. Rev. Lett.*, vol. 89, no. 16, Oct. 2002, Art. no. 167901.
[31] F. Grosshans, G.-W. Assche, J. Wenger, R. Brouri, N.-J. Cerf, and P. Grangier, "Quantum key distribution using Gaussian-modulated coherent states," *Nature*, vol. 421, pp. 238–241, Jan. 2003.
[32] J. Lodewyck et al., "Quantum key distribution over 25 km with an all-fiber continuous-variable system," *Phys. Rev. A*, vol. 76, no. 4, Oct. 2007, Art. no. 042305.
[33] P. Jouguet, K.-J. Sébastien, A. Leverrier, P. Grangier, and E. Diamanti, "Experimental demonstration of long-distance continuous-variable quantum key distribution," *Nature Photon.*, vol. 7, pp. 378–381, Apr. 2013.
[34] D. Huang et al., "Continuous-variable quantum key distribution with 1 Mbps secure key rate," *Opt. Exp.*, vol. 23, no. 13, pp. 17511–17519, Jun. 2015.
[35] D. Huang, P. Huang, D.-K. Lin, C. Wang, and G.-H. Zeng, "High-speed continuous-variable quantum key distribution without sending a local oscillator," *Opt. Lett.*, vol. 40, no. 16, pp. 3695–3698, Aug. 2015.
[36] X.-Y. Wang, W.-Y. Liu, P. Wang, and Y.-M. Li, "Experimental study on all-fiber-based unidimensional continuous-variable quantum key distribution," *Phys. Rev. A*, vol. 95, no. 6, Jun. 2017, Art. no. 062330.
[37] Y.-C. Zhang et al., "Long-distance continuous-variable quantum key distribution over 202.81 km of fiber," *Phys. Rev. Lett.*, vol. 125, no. 1, Jun. 2020, Art. no. 010502.
[38] Y. Tian et al., "Experimental demonstration of continuous variable measurement device independent quantum key distribution over optical fiber," *Optica*, vol. 9, no. 5, pp. 492–500, May 2022.
[39] H. Hansen et al., "Ultrasensitive pulsed, balanced homodyne detector: Application to time-domain quantum measurements," *Opt. Lett.*, vol. 26, no. 21, pp. 1714–1716, Nov. 2001.
[40] N. Gisin, G. Ribordy, W. Tittel, and H. Zbinden, "Quantum cryptography," *Rev. Mod. Phys.*, vol. 74, no. 1, pp. 145–195, Jan. 2002.
[41] X.-B. Wang, "Beating the photon-number-splitting attack in practical quantum cryptography," *Phys. Rev. Lett.*, vol. 94, no. 23, Jun. 2005, Art. no. 230503.
[42] V. Scarani, H. Bechmann-Pasquinucci, N.-J. Cerf, M. Dušek, N. Lütkenhaus, and M. Peev, "The security of practical quantum key distribution," *Rev. Modern Phys.*, vol. 81, no. 3, pp. 1301–1350, Jul.-Sep. 2009.
[43] H.-K. Lo, M. Curty, and K. Tamaki, "Secure quantum key distribution," *Nature Photon.*, vol. 8, pp. 595–604, Jul. 2014.
[44] E. Diamanti, H.-K. Lo, B. Qi, and Z. Yuan, "Practical challenges in quantum key distribution," *Npj Quantum Inf.*, vol. 2, Nov. 2016, Art. no. 16025.
[45] S. Pirandola et al., "Advances in quantum cryptography," *Adv. Opt. Photon.*, vol. 12, no. 4, pp. 1012–1236, Dec. 2020.
[46] G.-H. Bennett and G. Brassard, "Quantum cryptography: Public key distribution and coin tossing," in *Proc. IEEE Int. Conf. Comput., Syst., Signal Process.*, Bangalore, India,, 1984, pp. 175–179.
[47] S. Wang et al., "Twin-field quantum key distribution over 830-km fibre," *Nature Photon.*, vol. 16, pp. 154–161, Jan. 2022.
[48] S.-K. Liao et al., "Satellite-to-ground quantum key distribution," *Nature*, vol. 549, pp. 43–47, Aug. 2017.
[49] K. Kikuchi, "Fundamentals of coherent optical fiber communications," *J. Lightw. Technol.*, vol. 34, no. 1, pp. 157–179, Jan. 2016.
[50] X.-L. Jin et al., "Balanced homodyne detection with high common mode rejection ratio based on parameter compensation of two arbitrary photodiodes," *Opt. Exp.*, vol. 23, no. 18, pp. 23859–23866, Sep. 2015.
[51] Y.-M. Chi et al., "A balanced homodyne detector for high-rate Gaussian-modulated coherent-state quantum key distribution," *New J. Phys.*, vol. 13, Jan. 2011, Art. no. 013003.
[52] Y.-R. Guo, H.-D. Lu, W.-N. Peng, J. Su, and K.-C. Peng, "Intensity noise suppression of a high-power single-frequency CW laser by controlling the stimulated emission rate," *Opt. Lett.*, vol. 44, no. 24, pp. 6033–6036, Dec. 2019.
[53] J.-Q. Liu, X.-Y. Wang, Z.-L. Bai, and Y.-M. Li, "High precision auto-balance of the time-domain pulsed homodyne detector," *Acta Physica Sinica*, vol. 65, no. 10, May 2016, Art. no. 100303.
[54] X.-Y. Wang, J.-Q. Liu, X.-F. Li, and Y.-M. Li, "Generation of stable and high extinction ratio light pulses for continuous variable quantum key distribution," *IEEE J. Quantum Electron.*, vol. 51, no. 6, Jun. 2015, Art. no. 5200206.
[55] B. Qi, P. Lougovski, R. Pooser, W. Grice, and M. Bobrek, "Generating the local oscillator "locally" in continuous-variable quantum key distribution based on coherent detection," *Phys. Rev. X*, vol. 5, no. 4, Oct. 2015, Art. no. 041009.
[56] X.-C. Ma, S.-H. Sun, M.-S. Jiang, and L.-M. Liang, "Local oscillator fluctuation opens a loophole for Eve in practical continuous-variable quantum-key-distribution systems," *Phys. Rev. A*, vol. 88, no. 2, Aug. 2013, Art. no. 022339.

Xu-Yang Wang received the Ph.D. degree in optics from Shanxi University, Taiyuan, China, in 2013. He is currently an Associate Professor with Shanxi University. His research interests include integrated photonics, quantum communications, and manipulation of quantum states in light fields.

Xu-Bo Guo is currently working toward the M.S. degree in optics with Shanxi University, Taiyuan, China. His research interests include homodyne detection and continuous-variable quantum key distribution.

Yan-Xiang Jia is currently working toward the Ph.D. degree in optics with Shanxi University, Taiyuan, China. Her research interests include integrated photonics and quantum communications.

Yu Zhang is currently working toward the Ph.D. degree in optics with Shanxi University, Taiyuan, China. Her research interests include quantum communications and quantum tomography.

Zhen-Guo Lu received the Ph.D. degree from Shanxi University, Taiyuan, China, in 2021. He is currently a Lecturer with Shanxi University. His research interests include field programmable gate arrays and quantum random number generation.

Jian-Qiang Liu received the Ph.D. degrees from Shanxi University, Taiyuan, China, in 2022. His research interests include field programmable gate arrays, optical design, and control system of continuous-variable quantum key distribution.

Yong-Min Li received the Ph.D. degree in optics from Shanxi University, Taiyuan, China, in 2003. Since 2003, he has been a Postdoctoral Fellow with the University of Tokyo, Tokyo, Japan, and a Visiting Fellow with Australian National University, Canberra, ACT, Australia. He is currently a Professor with Shanxi University. His research interests include quantum optics and quantum information.